

Dedicated

To

My Beloved Family

And My Preceptor


CERTIFICATE

It is certified that the work contained in the thesis titled "SYNTHESIS, CHARACTERIZATIONS AND PHYSICAL PROPERTIES OF OXIDE ION CONDUCTING ELECTROLYTE MATERIALS FOR SOLID OXIDE FUEL CELL APPLICATIONS" by "PRAGATI SINGH" (Roll No. 16171007), in partial fulfilment of the requirement for the award of degree of Doctor of Philosophy at Indian Institute of Technology (B.H.U), Varanasi is a record of her own work carried out under my supervision and guidance, and this work has not been submitted elsewhere for a degree.

It is further certified that the student has fulfilled all the requirements of Comprehensive Examination, Candidacy, and SOTA for the award of Ph.D. Degree.

Date: 30/12/2021

Place: Varanasi


30/12/2021
Supervisor

(Prof. Prabhakar Singh)

Dr. Prabhakar Singh
प्राचार्य/Professor
भौतिकी विभाग/Dept. of Physics
ए.पी.एस.ओ. कॉलेज/वि.पी.ओ. / IIT (BHU)
वाराणसी / Varanasi-221005

ABSTRACT

A study was made of the effect of the rate of stirring on the characteristics and physical properties of films prepared by casting from solutions of polyethylene glycol in water. The results show that the rate of stirring has a marked effect on the thickness of the films and on the rate of evaporation of the solvent. The rate of stirring also affects the rate of crystallization of the polymer in the films.

The authors are indebted to the National Science Foundation for the grant which supported this work.

[Signature]
1961

1961

Dr. [Name]
[Address]
[City, State, Zip]

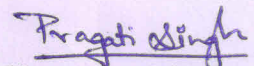
[Text]

DECLARATION BY THE CANDIDATE

I, **PRAGATI SINGH** (Roll No. 16171007), certify that the work embodied in this thesis is my own bonafide work and carried out by me under the supervision of **PROF. PRABHAKAR SINGH** from **JULY, 2016** to **DECEMBER, 2021** at the **DEPARTMENT OF PHYSICS**, Indian Institute of Technology, Varanasi. The matter embodied in this thesis has not been submitted for the award of any other degree/diploma. I declare that I have faithfully acknowledged and given credits to the research workers wherever their works have been cited in my work in this thesis. I further declare that I have not willfully copied from any other's work, paragraphs, text, data, results, *etc.*, reported in journals, books, magazines, reports dissertations, thesis, *etc.*, or available at websites and have not included them in this thesis and have not cited as my own work.

Date: 30/12/2021

Place: Varanasi





Signature of the Student

(PRAGATI SINGH)

CERTIFICATE BY THE SUPERVISOR

It is certified that the above statement made by the student is correct to the best of our knowledge.


30/12/2021
Supervisor
(Prof. Prabhakar Singh)
Dr. Prabhakar Singh
Professor
भौतिकी विभाग/Deptt. of Physics
भा० प्रौ० सं० / (का० हि० वि०) / IIT (BHU)
वाराणसी / Varanasi-221005


Signature of Head of Department
HEAD/विभागाध्यक्ष
भौतिकी विभाग/Deptt. of Physics
भा० प्रौ० सं० / (का० हि० वि०) / IIT (BHU)
वाराणसी / Varanasi-221005

COPYRIGHT TRANSFER CERTIFICATE

**Title of the Thesis: "Synthesis, Characterizations and Physical Properties of Oxide Ion
Conducting Electrolyte Materials for Solid Oxide Fuel Cell
Applications"**

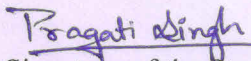
Name of the Student: Pragati Singh

Copyright Transfer

**The undersigned hereby assigns to the Indian Institute of Technology (Banaras Hindu
University) Varanasi all rights under copyright that may exist in and for the above thesis
submitted for the award of the "*Doctor of Philosophy*".**

Date: 30/12/2021

Place: IIT (BHU), Varanasi


Signature of the Student

(PRAGATI SINGH)

Note: However, the author may reproduce or authorize others to reproduce material extracted verbatim from the thesis or derivative of the thesis for author's personal use provided that the source and the Institute's copyright notice are indicated.

Acknowledgements

*It gives me immense pleasure to get an opportunity to express my heartfelt gratitude towards my respected supervisor, **Prof. Prabhakar Singh**, for his enthusiastic encouragement, guidance, support and valuable suggestions throughout my research work. His indomitable zeal and diligence towards work motivated me to bring some discipline in my own work so that I could systematically focus energy towards fulfilling my goal. I will always remain thankful to him.*

I would like to express my sincere thanks to my research progress evaluation committee (RPEC) members, Prof. Rajendra Prashad, Prof. Vinay Kumar Singh for the invaluable inspiration and numerous insightful suggestions during the entire course of this research. I offer my special thanks to Prof. Sandip Chatterjee, Head of the Department of Physics for extending experimental facilities during the entire course of this research work.

I wish to express deep regards to all the teachers of the Department Prof. B. N. Dwivedi, Prof. O. N. Singh, Prof. D. Giri, Prof. R. Prasad, Dr. P. C. Pandey, Dr. Anita Mohan, Dr. Shail Upadhyay, Dr. S. K. Mishra, Dr. A. K. Srivastava, Dr. S. K. Singh, Dr. Avanish Singh Parmar, Dr. Saurabh Tripathi, Dr. Awaneesh Singh, Dr. R. K. Singh, Dr. Swapnil Patil, Dr. Shradha Mishra, Dr. Prasun Dutta, Dr. Rajeev Singh, Dr. Somnath Nag, Dr. Gauhar Abbas, Dr. Bidya Binay Karak, Dr. P. K. Aluri for their kind support at all moment during the progress of my research.

With a deep sense of gratitude, I express my sincere thanks to CIFIC, IIT (BHU), Varanasi for help in carrying characterization of the synthesized samples. I am also grateful to all office staff of the Department and authorities of IIT (BHU), for their kind help during the period of my stay to complete the thesis work.

A special word of thanks goes to Dr. Raghvendra Pandey at the University of Delhi for his invaluable suggestions and scientific view in resolving lots of difficulties I faced during my research work.

I would also like to express my extreme gratefulness towards my senior research members Dr. N. K. Singh, Dr. R. K. Singh, Dr. B. P. Singh, Dr. Pravin Kumar, Dr. Priyanka A. Jha, Dr. Pardeep Jha, Dr. Priyam Singh, Dr. Ashutosh Sahi, Dr Pawan Dubey, Dr. Onkar Nath Verma, Dr. Saurabh Singh, Dr. Vani Pawar and labmates, Mr. Ashish Kumar Yadav, Mr. Manish Kumar, Mr. Ajay Shankar Bangwal, Ms. Vandna Tomar, Ms. Manisha Chauhan, Ms. Swarnima Singh, Mr. Prem Chandra Bharti, Ms. Uma Sharma, Ms. Manisha Sharma, Ms. Gargi Yadav, Mr. Jaynarayan Mishra, Ms. Kamana Mishra, and all research colleagues of Department of Physics, IIT(BHU), for sharing their knowledge and creating enjoyable lab atmosphere both on and off the slopes. Special thanks are due to all the my departmental research colleagues for the help and their awesome company for giving me moral support, pleasant company and confidence to complete my work with a 'smile'.

The cooperation, moral support and constant motivation which I have always received from my friends cannot be expressed in words and I feel lucky to be blessed with such wonderful friends. Some of them who deserve special thanks are Mr.

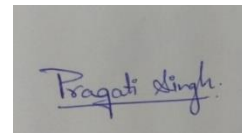
Sudheer Kumar Mishra, Mr. Rajneesh Dwivedi, Ms. Kanchan Yadav, Ms. Pratibha Verma, and Ms. Aparajita Paul.

The biggest source of inspiration and courage was my entire family, whose boundless love, constant emotional support and blessings have provided me encouragement at every step of life. I infinitely cherish my parents for dreaming my dreams, always being there and bearing the burden of me staying away from them. The journey would not have been possible without the most special person I know, my husband, whom I am so grateful towards for his extraordinary ability to support, reason and lead my way in the right trajectory.

Finally, I bow with reverence and gratitude to thank the Almighty who has enriched me with such an excellent opportunity and infused the power in my mind to fulfil the work assigned to me.

Date: 30\12\2021

Place: Varanasi

A rectangular box containing a handwritten signature in blue ink that reads "Pragati Singh".

(Pragati Singh)

Contents

Certificate	iii
Declaration by the Candidate	v
Copyright Transfer Certificate	vii
Acknowledgements	viix
Contents	xi
List of Figures	xvii
List of Tables	xxvii
List of Symbols and Abbreviations	xxix
Preface	xxxiii
CHAPTER 1: Introduction and Literature Review	1
1.1 Introduction	1
1.2 Fuel Cells: An Overview	3
1.2.1 Fuel Cell Efficiency	4
1.2.2 Fuel cell voltage	6
1.3 Fuel Cell Types	7
1.4 Solid oxide fuel cell (SOFC)	10
1.5 Operation Principle	11
1.6 Components of SOFC	13
1.6.1 Oxygen electrode (Cathode)	13
1.6.2 Fuel electrode (Anode)	14
1.6.3 Interconnect	14
1.6.4 Electrolyte	15
1.7 Factors influencing the ionic conductivity of an electrolyte	18
1.7.1 Conduction Process	19

1.7.2 Microstructural Control	23
1.8 Present scenario of electrolyte materials for solid oxide fuel cell.....	26
1.9 Materials for electrolytes.....	28
1.9.1 Fluorite structured electrolyte.....	28
1.9.2 Brownmillerite – type ceramics.....	31
1.9.3 La ₂ Mo ₂ O ₉ (LAMO _X) based electrolyte materials.....	33
1.9.4 Apatite structure.....	35
1.9.5 Perovskite-based ceramics.....	36
1.9.6 Sodium Bismuth Titanate (Na _{0.5} Bi _{0.5} TiO ₃).....	39
1.9.7 Pyrochlores based ceramics	40
1.9.8 δ-Bi ₂ O ₃ based ceramics	41
1.10 Tri-Yttrium Gallate (Y ₃ GaO ₆).....	43
1.11 Objective of the Present Research Work.....	45
CHAPTER 2: Synthesis, Characterizations and Analysis Techniques	47
2.1 Overview	47
2.1.1 Specification of Raw Materials	48
2.2 Materials Synthesis	49
2.2.1 Solid-State Reaction Route (SSR).....	49
2.2.2 Polyol-mediated synthesis route	50
2.3 Pelletization for Conductivity and Dilatometry Measurements	52
2.4 Characterization Techniques	53
2.4.1 Thermal Analysis (TGA-DTA)	53
2.4.2 X-Ray Diffraction Analysis (XRD).....	55
2.4.3 Bragg's law.....	55
2.4.4 Fourier Transform Infrared Spectroscopy (FTIR).....	58
2.4.5 Dilatometry	59
2.4.6 BET Surface Area Measurements	61

2.4.7 Raman Spectroscopy	62
2.4.8 X-Ray Photoelectron Spectroscopy (XPS)	65
2.4.9 Scanning Electron Microscopy (SEM)	67
2.4.10 Ultra-Violet Visible (UV-Vis) Spectroscopy	69
2.4.11 Photoluminescence Spectroscopy (PL)	70
2.4.12 Density Measurement	72
2.5 Electrical Data Analysis	73
2.5.1 Impedance Spectroscopy Analysis	75
2.5.2 Conductivity Spectroscopy Technique	80
2.6 Analysis Techniques	82
2.6.1 Rietveld Refinement Technique	82
2.6.2 Process of Analyzing the Obtained Data	87
2.7 Theoretical Studies	87
2.7.1 Bond Valance Energy-Based Approach	87
CHAPTER 3: Effect of Sintering Temperature on Ion Dynamics of Na_{0.5}Bi_{0.5}TiO₃.....	89
3.1 Introduction	89
3.2 Experimental Procedure	90
3.3 Results and Discussion.....	91
3.3.1 Structural Studies.....	91
3.3.2 AC Conductivity Formalism.....	93
3.3.3 Scaling Mechanism.....	98
3.3.4 Differential Impedance Analysis	101
3.3.5 Correlation of structural and electrical behaviour	103
3.3.6 Stability under reducing atmosphere	106
3.4 Conclusion.....	107
CHAPTER 4: Ion Dynamics of Non-Stoichiometric Na_{0.5+x}Bi_{0.5-x}TiO_{3-δ}: A Degradation Study.....	109
4.1 Introduction	109

4.2 Experimental Procedure	110
4.3 Results and Discussion.....	111
4.3.1 Structural Studies.....	111
4.3.2 Microstructural Analysis	114
4.3.3 X-ray Photoelectron Spectroscopy Analysis	115
4.3.4 Thermogravimetric Analysis (TGA)	120
4.3.5 AC Conductivity Formalism.....	121
4.4 Degradation Mechanism.....	124
4.4.1 Structural Properties Before and After Reduction.....	124
4.4.2 Electrical Properties before and after reduction	126
4.5 Conclusion.....	134
CHAPTER 5: Investigation of Oxide Ion Migration in Bi-deficient Mg²⁺ Doped Sodium Bismuth Titanate.....	135
5.1 Introduction.....	135
5.2 Experimental Procedure	136
5.3 Results and Discussion.....	137
5.3.1 Structural Analysis.....	137
5.3.2 Migration Pathway Analysis.....	141
5.3.3 Surface Morphology Study	145
5.3.4 FTIR Study	146
5.3.5 Thermogravimetric Analysis	147
5.3.6 Raman Spectroscopy Study	148
5.3.7 Brunauer- Emmett-Teller (BET) Analysis	151
5.3.8 Electrical Conductivity Study	153
5.4 Conclusion.....	156
CHAPTER 6: Oxide-ion conduction in alkaline earth metal doped Y₃GaO₆: Substitution on A site.....	159
6.1 Introduction.....	159

6.2 Experimental Procedure	160
PART A	162
Oxide Ion Conduction in Alkaline Earth Metal Doped Y_3GaO_6.....	162
6.3 Results and Discussion.....	162
6.3.1 Structural Analysis.....	162
6.3.2 Conductivity Analysis	169
6.3.3 Photoluminescence (PL) Analysis	176
6.3.4 UV-Vis Analysis.....	177
6.3.5 FTIR Analysis.....	178
6.3.6 SEM Analysis	179
6.3.7 Thermal Expansion Study.....	180
6.4 Conclusion.....	183
PART B.....	162
Examining the consequences of calcium substitution on the structural and electrical properties of Y_3GaO_6.....	184
6.5 Results and Discussion.....	184
6.5.1 Structural Studies.....	184
6.5.2 Surface morphology and density	189
6.5.3 UV-Vis Analysis.....	190
6.5.4 Impedance Analysis.....	191
6.5.5 Electron density map	194
6.5.6 PL Analysis.....	197
6.5.7 Scaling behaviour and conduction mechanism.....	199
6.5.8 Cyclic Voltammetry.....	200
6.6 Conclusions	202
CHAPTER 7: Conclusions and Future Scopes.....	205
7.1 Conclusion of the Present Investigation.....	205
7.2 Outlook for Future Perspective	207

References..... 211
List of Publications 230

LIST OF FIGURES

		Page No.
Chapter I	Introduction and Literature review	
Fig. 1.1	(a) World energy consumption by different energy sources with projection from 2010 to 2050. (b) Energy consumption by fuel type	2
Fig. 1.2	William Groves battery diagram	4
Fig. 1.3	Maximum efficiency of hydrogen fuel cell with the steam produced compared to Carnot limit with 50 °C exhaust temperature	5
Fig. 1.4	Plot indicating for a low temperature fuel cell fed with air and hydrogen	7
Fig. 1.5	Reactions at electrodes for different types of fuel cells	10
Fig. 1.6	Schematic of working principle of (a) oxide ion conducting (b) proton-conducting SOFC	12
Fig. 1.7	Schematic of ion diffusion mechanism (a) vacancy diffusion (b) Interstitial diffusion (c) ions exchange in solid state structure	17
Fig. 1.8	Comparative of bulk conductivity of prominent oxide ion conductors	18
Fig. 1.9	(a) Sources of ionic carriers in oxides (b) Correlation between composition, microstructure, processing, and electrical conductivity of polycrystalline materials	19
Fig. 1.10	Present scenario of electrolyte materials	28
Fig. 1.11	Fluorite structure	29
Fig. 1.12	Brownmillerite crystal structure	33
Fig. 1.13	Comparison of the cationic environment of β -SnWO ₄ and β -La ₂ Mo ₂ O ₉	34
Fig. 1.14	Structural defects position and conduction mechanism	36

Fig. 1.15	(a) Perovskite structure ABO_3 (b) Schematic of the curved pathway of oxide ion migration along the BO_6 octahedron (c) Saddle point configuration of oxide ion migration showing relaxation	37
Fig. 1.16	Visualization of δ - Bi_2O_3 unit cell	41
Fig. 1.17	Crystal structure of Y_3GaO_6 along 001 direction showing GaO_4 tetrahedra. Green, red and blue sphere represents the Y^{3+} , O^{2-} , and Ga^{3+} ions, respectively. Y1 and Y2 of the crystallographic positions of Y	44
Chapter II	Synthesis, Characterizations and Analysis Techniques	
Fig. 2.1	Schematic of Solid-state reaction route	50
Fig. 2.2	Schematics of polyol mediated synthesis process	52
Fig. 2.3	Experimental setup of hydraulic press machine	53
Fig. 2.4	(a) The schematic representation and (b) experimental setup of TGA/DSC (right) [Central instrument facility (CIF) IIT (BHU)]	54
Fig. 2.5	(a) Visualization of Bragg's law (b) Schematic representation of $\theta/2\theta$ diffraction in Bragg-Brentano geometry	56
Fig. 2.6	Experimental setup of X-ray diffractometer CIF IIT (BHU) [Rigaku Miniflex II, Japan].	57
Fig. 2.7	(a) Mechanism and (b) experimental setup of Fourier transform infrared spectroscopy	58
Fig. 2.8	Experimental setup of Dilatometry for TEC measurement [NETZSCH DIL, 402 PC/4]	60
Fig. 2.9	(a) Mechanism and (b) Experimental setup of porosity and BET surface area analyzer [Micromeritics ASAP 2020]	62
Fig. 2.10	Schematic representation of the principle of Raman spectroscopy	64
Fig. 2.11	Experimental setup of DXRxi Raman measurement	65
Fig. 2.12	(a) Mechanism and (b) Experimental setup for the XPS spectroscopy (Kratos Amicus)	66

Fig. 2.13	(a) Mechanism and (b) Experimental setup of SEM measurement (CIF-IIT (BHU))	68
Fig. 2.14	Experimental setup of UV-Visible measurement [JASCO V-770 UV-Vis spectrometer]	70
Fig. 2.15	(a) Mechanism and (b) Experimental setup of photoluminescence spectroscopy	72
Fig. 2.16	Density measurement kit by Sartorius, BSA2245-CW	73
Fig. 2.17	Experimental set up of automated impedance analyzer along with sample holder and furnace (6500 P Wayne Kerr, UK)	74
Fig. 2.18	Experimental set up of automated impedance analyzer along with sample holder and furnace (6500 P Wayne Kerr, UK)	79
Fig. 2.19	A typical conductivity spectra of a polycrystalline material	81
Fig. 2.20	A typical FullProf software interface during the Rietveld refinement process	84
Chapter III	Effect of Sintering Temperature on Ion Dynamics of $\text{Na}_{0.5}\text{Bi}_{0.5}\text{TiO}_3$	
Fig. 3.1	(a) Rietveld refinement of XRD pattern for different sintering temperatures (b) FTIR of the sample sintered at 1100 °C	91
Fig. 3.2	Depicts the variation of $\log \sigma$ vs $\log \nu$ from 500 °C to 700 °C at the step of 20 °C for the samples synthesized under different sintering temperatures (a) 1000 °C (b) 1050 °C (c) 1100 °C (d) 1150 °C	94
Fig. 3.3	(a) Variation of $\log \sigma_{dc}$ vs $\log \nu_h$ (b) Arrhenius plot for estimation of activation energy for the samples synthesized under different sintering temperatures, (c) Variation of E_a with sintering temperature and (d) SEM micrographs of the samples sintered at different sintering temperatures and respective insets shows their grain size histograms	94
Fig.3.4	Variation of 'n' with temperature for the samples synthesized under different sintering temperatures	96
Fig.3.5	Variation of charge carrier concentration factor 'N' with temperature for the samples synthesized under different sintering temperatures	98
Fig.3.6	Ghosh scaling for the samples synthesized under different sintering temperatures	99

Fig. 3.7	Summerfield scaling for the samples synthesized under different sintering temperatures	100
Fig. 3.8	Modulus scaling (M''/M''_{\max} vs ν/ν_{\max}) with the variation of sintering temperature (a) 1000 °C (b) 1050 °C (c) 1100 °C (d) 1150 °C	100
Fig. 3.9	Variation of Na/Bi-Ti bond with the sintering temperature (inset) structure of NBT from Diamond	101
Fig. 3.10	Estimation of K using relation $ Z _{adj} = f^{-K}$ from $\log Z $ vs $\log \nu$ for all the studied samples	102
Fig. 3.11	Variation of K with temperature ranging from 500 °C to 700 °C for all the studied samples	103
Fig. 3.12	(a) Normalized M'' and Z'' isotherms with frequency in the temperature range of 500 °C to 700 °C with the variation of sintering temperature (b) Variation of relaxation hopping frequency with temperature for the samples sintered at 1000 °C and 1150 °C (c) Range of $\Delta\nu_r$ for all the studied samples	103
Fig. 3.13	(a) Plot of XRD intensity of peak ($2\theta \sim 32^\circ$) vs $2\theta - \delta$ ($^\circ$) where δ is the angle at which maxima occurs showing diffuseness of XRD peak with the sintering temperature, (b) Variation of coherence length, L_{coh} and lattice constant, a with the sintering temperature	105
Fig. 3.14	X-ray diffractograms of the NBT sample and the sample dipped in propan-2-ol ($\text{C}_3\text{H}_7\text{OH}$) for two days (i) $\log \sigma$ vs $\log \nu$ for the NBT sample and sample dipped in propan-2-ol (ii) Modulus Nyquist plots at room temperature for the NBT sample and sample dipped in propan-2-ol (iii) Gray highlighted region of inset (ii) showing modulus Nyquist plots of pure NBT sample at room temperature	107
Chapter IV	Ion Dynamics of Non-Stoichiometric $\text{Na}_{0.5+x}\text{Bi}_{0.5-x}\text{TiO}_{3-\delta}$: A Degradation Study	
Fig. 4.1	X-ray diffractograms of the $\text{Na}_{0.5+x}\text{Bi}_{0.5-x}\text{TiO}_{3-\delta}$ ($x = -0.02, -0.01, 0.0, 0.01$ and 0.02) compositions	111
Fig. 4.2	Rietveld refined X-ray diffractograms of the studied $\text{Na}_{0.5+x}\text{Bi}_{0.5-x}\text{TiO}_{3-\delta}$ ($x = -0.02, -0.01, 0.0, 0.01$ and 0.02) compositions	112
Fig. 4.3	Volume and tolerance factor of the studied $\text{Na}_{0.50+x}\text{Bi}_{0.50-x}\text{TiO}_{3-\delta}$ ($x = -0.02, -0.01, 0.0, 0.01$ and 0.02) compositions	114

Fig. 4.4	SEM micrographs of the studied $\text{Na}_{0.5+x}\text{Bi}_{0.5-x}\text{TiO}_{3-\delta}$ ($x = -0.02, -0.01, 0.0, 0.01$ and 0.02 , (a-e)) compositions	115
Fig. 4.5	Wide range X-Ray photoelectron spectra of $\text{Na}_{0.5+x}\text{Bi}_{0.5-x}\text{TiO}_{3-\delta}$ ($x = -0.02, 0.00, 0.01$ and 0.02) compositions showing the presence of Na, Bi, Ti and O	117
Fig. 4.6	X-ray photoelectron spectroscopy measurements (deconvoluted peaks) of the studied $\text{Na}_{0.5+x}\text{Bi}_{0.5-x}\text{TiO}_{3-\delta}$ ($x = -0.02, 0.0, 0.01$ and 0.02) compositions	117
Fig. 4.7	Depicts the Na/Bi ratio and grain size obtained from XPS and grain histograms, respectively	119
Fig. 4.8	Thermogravimetric analysis of the studied $\text{Na}_{0.5+x}\text{Bi}_{0.5-x}\text{TiO}_{3-\delta}$ ($x = -0.01, 0.0$ and 0.01) compositions	120
Fig. 4.9	(a) Variation of $\log \sigma$ vs $\log \nu$ for $x = 0.0$ sample (for instance), (b) Variation of exponent with temperature, (c) Variation of $\log \sigma_{dc}$ vs $\log \nu_h$ and (d) Arrhenius fitting of conductivity	123
Fig. 4.10	(a) Comparative of X-ray diffractograms of the fresh and reduced samples and (b) Visualization of unit cell structure of fresh and reduced sample of composition with $x = 0$	124
Fig. 4.11	Comparative of $\log \sigma$ vs $\log \nu$ of the fresh and reduced $x = 0.0$ sample	127
Fig. 4.12	Comparative of $\ln \sigma$ vs $1000/T$, exponent vs temperature with error bars and $\log \sigma_{dc}$ and $\log \nu_h$ of the fresh and reduced $x = -0.01, 0.0$ and 0.01 samples	128
Fig. 4.13	Comparative of $\log \tau_o$ vs x of the fresh and reduced $x = -0.01, 0.0$ and 0.01 samples, (inset) Linear fitting of $\log \nu_h$ vs $1000/T$ of the fresh $x = -0.01, 0.0$ and 0.01 samples	129
Fig. 4.14	Variation of the value of concentration of mobile charge ions with temperature of the fresh and reduced $x = -0.01, 0.0$ and 0.01 samples	130
Fig. 4.15	Variation of $\tan \delta$ with temperature of the fresh and reduced $x = -0.01, 0.0$ and 0.01 samples	131
Fig. 4.16	Thermogravimetric analysis of the reduced $\text{Na}_{0.5+x}\text{Bi}_{0.5-x}\text{TiO}_{3-\delta}$ ($x = -0.01, 0.0$ and 0.01) compositions	132
Chapter V	Investigation of Oxide Ion Migration in Bi-deficient Mg^{2+} Doped Sodium Bismuth Titanate	

Fig. 5.1	(a) X-ray diffractogram pattern of $\text{Na}_{0.5}\text{Bi}_{0.49}\text{Ti}_{(1-x)}\text{Mg}_{(x)}\text{O}_{3-\delta}$ ($x = 0.00, 0.01, 0.02, 0.03$) (b) Representative crystal structure in 3D view	138
Fig. 5.2	Rietveld refinement pattern of NBT4900, NBT4901, NBT4902 and NBT4903. Black circles represent the experimental data, and red lines are the fit.	139
Fig. 5.3	(a) Variation of lattice parameters a , c and, volume (b) Octahedral tilting (ϕ) with composition obtained from Rietveld refinement	140
Fig. 5.4	(i) Bond valence energy landscape (BVEL) of all the investigated system at the iso-surface value 2.5 eV (ii) Oxide ion migration channel of studied composition in the b-c plane obtained from BVE method.	142
Fig. 5.5	(a-d) Oxide ion diffusion energy migration barrier landscape for NBT4900, NBT4901, NBT4902 and NBT4903, respectively. All the sample are showing 3D migration channel except NBT4903 in which 2D migration is predominating (e) A representative BVEL of NBT4902 unit cell	144
Fig. 5.6	SEM Micrographs of the sintered samples. Inset shows grain size distribution histogram	145
Fig. 5.7	FTIR spectrum of $\text{Na}_{0.5}\text{Bi}_{0.49}\text{Ti}_{(1-x)}\text{Mg}_{(x)}\text{O}_{3-\delta}$ ($x = 0.00, 0.01, 0.02, 0.03$)	146
Fig. 5.8	TGA of $\text{Na}_{0.5}\text{Bi}_{0.49}\text{Ti}_{(1-x)}\text{Mg}_{(x)}\text{O}_{3-\delta}$ ($x = 0.00, 0.01, 0.02, 0.03$) in N_2 atmosphere	148
Fig. 5.9	Room temperature Raman spectra of the studied compositions	149
Fig. 5.10	Deconvoluted Raman spectra using 13 peaks showing the presence of R3c symmetry	150
Fig. 5.11	FWHM variation in Raman spectra for E(TO4) and E(LO9) mode of all the investigated compositions	151
Fig. 5.12	BET nitrogen adsorption isotherm as a function of relative pressure	152
Fig. 5.13	(a) Representative AC impedance spectra at 500 °C (b) Arrhenius plot for total conductivity (c) Variation of	155

migration barrier and activation energy for $\text{Na}_{0.5}\text{Bi}_{0.49}\text{Ti}_{(1-x)}\text{Mg}_{(x)}\text{O}_{3-\delta}$ ($x = 0.00, 0.01, 0.02, 0.03$)

Chapter VI	Oxide-ion conduction in alkaline earth metal doped Y_3GaO_6: Substitution on A site	
Fig. 6.1	(a) Room-temperature XRD pattern of the studied samples and XRD of Y_3GaO_6 taken from ICSD database (b) 3D polyhedral representation of crystal structure	164
Fig. 6.2	Rietveld refined patterns with observed (black circles), calculated (solid red line), Bragg reflections (green vertical ticks) and (blue line) difference profiles for the studied compositions sintered at 1350 °C for 6h	164
Fig. 6.3	(a) Schematic of the energy barrier landscape of single oxide ion migration inside the crystal lattice (b) Crystal structure, including migration iso-surface of at 2.7 eV in Y_3GaO_6 . Yellow colour represents the iso-surface.	166
Fig. 6.4	(a-b) Bond valance energy landscape for oxide ion migration viewed along c axis with various iso-surface. Yellow iso-surface in Fig. (a) represents the presence of migration pathway and the rejected iso-surface in Fig. (b) represents the absence of migration channel. The energy difference between fig. a and b gives the Energy barrier E_b for migration at room temperature (c) Energy barrier histogram at room temperature for studied compositions.	167
Fig. 6.5	Oxygen ion diffusion iso-surface channel of YGO and YCGO along c-axis at (a) 2.80 eV (b) at 3.90 eV derived from the bond valance energy landscape using VESTA software.	168
Fig. 6.6	(a) Complex Impedance plot of studied compositions at 600 °C in the air. (b) Complex Impedance plot for YCGO and YSGO sample. (c) Arrhenius plot (Variation of $\log [\sigma_{\text{bulk}}*T]$ with the inverse of temperature) of the studied compositions with the inversed of temperature.	172
Fig. 6.7	Dependence of (a) total conductivity (b) oxide ion conductivity on the dopant ionic radii at 700 °C	173
Fig. 6.8	Intrinsic strain developed inside the crystal due to defects, grain boundary and faults calculated using Williamson-Hall analysis	175

Fig. 6.9	Oxygen partial-pressure dependence of total electrical conductivity of YGO, YCGO, and YSGO samples at (a) 700 and (b) 800 °C, respectively.	175
Fig. 6.10	Room temperature photoluminescence spectra under an excitation wavelength of 260 nm and slit width 1nm	176
Fig. 6.11	(a) Tauc's plot for direct band-gap calculation of YGO, YCGO, YSGO and YBGO samples. (b) Corresponding band structure.	177
Fig. 6.12	Room temperature FTIR spectra of YGO, YCGO, YSGO and YBGO samples. Figure in the inset shows the decrease in the metal-oxygen bond intensity with the increase in the atomic mass of dopant	179
Fig. 6.13	(a-d) SEM Micrographs of YGO, YCGO, YSGO and YBGO samples. Inset in the figure shows grain size distribution (e) Grain size variation of the studied compositions	180
Fig. 6.14	Thermal expansion curve of YGO, YCGO and YSGO compositions from Room temperature to 1000 °C	182
Fig. 6.15	(a) XRD patterns of studied compositions (b) Crystal structure of Y_3GaO_6	185
Fig. 6.16	The percentage of phase purity with the increase in calcium concentration in Y_3GaO_6	187
Fig. 6.17	(a) Rietveld refinement fit pattern of all the studied systems (b) Full structure refinement of 0Ca and 2Ca composition.	188
Fig. 6.18	(a-c) Variation of lattice parameters and volume with dopant concentration for orthorhombic (Y_3GaO_6), cubic (Y_2O_3) and triclinic ($CaCO_3$) phases, respectively (d) Oxygen percentage change for all the compositions analyzed from Rietveld refinement and SEM-EDX studies.	189
Fig. 6.19	(a-e) SEM micrographs of $Y_{3(1-x)}Ca_{3x}GaO_6$ ($x = 0, 0.02, 0.04, 0.08, 0.12$) compositions.	189
Fig. 6.20	Tauc plot showing the variation of $(\alpha h\nu)^2$ vs $h\nu$ with dopant concentration	191
Fig. 6.21	(a) Impedance Nyquist plot at 700 °C. Inset depicts the equivalent circuit to fit the impedance spectra along with impedance plot of Ca doped compositions (b) Arrhenius plot	193

	for total conductivity of studied compositions. Inset depicts the conductivity histogram at 700 °C	
Fig. 6.22	Arrhenius plot for (a) grain (b) grain-boundary conductivity of studied compositions	194
Fig. 6.23	Electron density contour map of all studied compositions in the z-y plane	196
Fig. 6.24	Space charge ionic fitting model for all the studied specimens	197
Fig. 6.25	(a-b) Room temperature photoluminescence spectra with an excitation wavelength of 305 nm	198
Fig. 6.26	Modulus scaling behaviour for all the samples at different temperatures	199
Fig. 6.27	(a-b) Cyclic voltammogram curve with the various scan rate (c) Specific capacitance at different scan rate for 0Ca and 2Ca sample (d) Chronoamperometry plot of undoped Y_3GaO_6 sample at 1.5 V	201

LIST OF TABLES

		Page No.
Chapter I	Introduction and Literature review	
Table 1.1	Different types of fuel cells with their characteristics	9
Chapter II	Synthesis, Characterizations and Analysis Techniques	
Table 2.1	Description of the raw materials with their chemical formula, purity, and manufacturer used for the preparation of proposed compositions	48
Chapter III	Effect of Sintering Temperature on Ion Dynamics of $\text{Na}_{0.5}\text{Bi}_{0.5}\text{TiO}_3$	
Table 3.1	Atomic positions and R-factors obtained after refinement for the $\text{Na}_{0.5}\text{Bi}_{0.5}\text{TiO}_3$ samples sintered at different temperature	92
Chapter IV	Ion Dynamics of Non-Stoichiometric $\text{Na}_{0.5+x}\text{Bi}_{0.5-x}\text{TiO}_{3-\delta}$: A Degradation Study	
Table 4.1	Lattice parameters, atomic positions and goodness of fitting parameters of the studied $\text{Na}_{0.5+x}\text{Bi}_{0.5-x}\text{TiO}_{3-\delta}$ ($x = -0.02, -0.01, 0.0, 0.01$ and 0.02 compositions)	113
Table 4.2	Area of the peaks obtained from XPS peak fitting	118
Table 4.3	δ obtained from TGA and XPS	121
Table 4.4	Lattice parameters, atomic positions and goodness of fitting parameters of the studied $\text{Na}_{0.5+x}\text{Bi}_{0.5-x}\text{TiO}_{3-\delta}$ ($x = -0.01, 0.0, 0.01$) compositions after reducing	125
Table 4.5	Lattice parameters, atomic positions and goodness of fitting parameters of the sample dipped in propanol for 48h	125
Chapter V	Investigation of Oxide Ion Migration in Bi-deficient Mg^{2+} Doped Sodium Bismuth Titanate	
Table 5.1	Position coordinates and Rietveld fitting parameters and for all the studied samples	140
Table 5.2	Average crystallite size, micro-strain and density of the investigated compositions	141
Table 5.3	Oxygen vacancy estimated from TGA data and electrical conductivity	148

Table 5.4	BET surface area, pore size and pore volume of all investigated compositions	152
Chapter VI	Oxide-ion conduction in alkaline earth metal doped Y_3GaO_6: Substitution on A site	
Table 6.1	Rietveld refined lattice parameters, volume, density and porosity of the studied compositions	163
Table 6.2	Value of grain, grain-boundary capacitance, total conductivity at 600 °C, and activation energy of studied compositions	170
Table 6.3	Bonding strength with the oxygen of di-valent A-site dopant	173
Table 6.4	TEC of the measured sample between room temperature and 1000 °C	182
Table 6.5	Crystallite size, lattice strain, density and FWHM of the studied samples	188
Table 6.6	Energy band gap	191
Table 6.7	Comparison of grain, grain-boundary conductivity and activation energy of Ca doped samples	194

LIST OF SYMBOLS AND ABBREVIATIONS

SOFC	Solid Oxide Fuel Cell
PEMEC	Proton Exchange Membrane Fuel Cell
AFC	Alkaline Fuel Cell
PAFC	Phosphoric Acid Fuel Cell
MCFC	Molten Carbonate Fuel Cell
HT-SOFC	High Teemperature Solid Oxide Fuel Cell
IT-SOFC	Intermediate Temperature Solid Oxide Fuel Cell
LT-SOFC	Low Temperature Solid Oxide Fuel Cell
NBT	Sodium Bismuth Titanate
YGO	Tri-yttrium Gallate
YBGO	Barium doped YGO
YCGO	Calcium doped YGO
YSGO	Strontium doped YGO
VB	Valance Band
CB	Conduction Band
eV	Electron Volt
meV	Milli-electron Volt
E_g	Band Gap
E_a	Activation Energy
$h\nu$	Photon Energy
k_B	Boltzmann's constant
FWHM	Full Width at Half Maximum
G	Gram
K	Kelvin

M.P.	Melting Point
T	Temperature
ICDD	International Center for Diffraction Data
JCPDS	Joint Committee on Powder Diffraction Standards
VSEPR	Valence Shell Electron Repulsion Theory
M	Modulus
Z, Z', Z''	Complex, real and imaginary impedance
Σ	Conductivity
T	Relaxation time
Ω	Angular frequency ($2\pi f$)
θ	Diffraction angle
CV	Cyclic Voltammetry
PL	Photoluminescence Spectroscopy
ΔG	Gibbs Free Energy
ΔS	Entropy
ΔH	Enthalpy
RT	Room Temperature
\AA	Angstrom
mg	Milligram
N	Avogadro's Number
nm	Nanometer
cm	Centimetre
μm	Micro-meter
Pt	Platinum
mV	MilliVolt
Ag	Silver
TEC	Thermal Expansion Coefficient

SSR	Solid State Route
SEM	Scanning Electron Microscope
TEM	Transmission Electron Microscopy
XPS	X-Ray Photoelectron Spectroscopy
UV-Vis	Ultraviolet-Visible
DSC	Differential Scanning Calorimetric
CPE	Constant Phase Element
XRD	X-ray Diffraction
TGA	Thermogravometric Analysis
BVE	Bond Valance Sum
BVELs	Bond Valance Energy Landscape

PREFACE

Global energy demand is continually rising as a result of ongoing industrial development and population increase. The demand for energy, particularly from liquid fuels, has generated a bottleneck since the early 2000s, resulting in the current energy crisis. The combustion of fossil fuels provides the majority of the energy needed to the world. As a result, the globe is dealing with a variety of issues, including climate change, oil spills, air pollution, acid rain, and so on. Alternatively, wind, solar and hydro-power systems are rapidly growing and gaining popularity all over the world. However, because these renewable energy sources are generally dependent on the weather, their extensive expansion is limited. Wind turbines need wind to turn on their blades, and solar collectors need sunlight to gather heat and generate power. The current cost of renewable energy technology is also far in excess of traditional fossil fuel generation. Furthermore, they are less efficient and non-portable. To address these constraints, ongoing attempts are being made to produce superior, highly efficient, and long-term energy conversion systems. Fuel cell is one of the promising technologies that is expected to meet the majority of these requirements.

A fuel cell is an electrochemical device that converts chemical energy contained in fuels (such as hydrogen, methane, butane, etc.) into electrical energy by exploiting the natural tendency of oxygen and hydrogen to react. High efficiency and fuel adaptability are not the only major advantages of fuel cells, but they are also attractive as they are clean, reliable and almost non-polluting. Furthermore, since there are no moving parts, they are vibration-free. Fuel cells are classified on the basis of the electrolyte they employ. Among them, it has been favoured to choose solid oxide fuel cell (SOFC) because of its durability, portability, and high

efficiency. Furthermore, SOFCs are less sensitive to fuel contaminants. SOFC consists of anode, cathode, electrolyte, interconnect and seal. The electrolyte, which is sandwiched between the cathode and anode, is critical to the SOFC's operation. It must have appropriate oxygen-ion conductivity, minimal electrical conductivity, stability in both oxidizing and reducing conditions, and the ability to remain dense and impermeable while the cell is operating. Among all the investigated electrolyte materials, yttria-stabilized zirconia (YSZ) is the most extensively used electrolyte. However, the use of YSZ is restricted due to the electrical conductivity's limiting magnitude and its high operating temperature of over 800 °C. It becomes increasingly important to reduce the operating temperature of the fuel cells down in order to prolong the life span of a cell, the stability of a SOFC, widen the selection of electrodes, interconnect and manifold materials and also to reduce the overall cost of material processing & cell fabrication.

Our present work is focused on the development of the electrolyte materials for intermediate temperature SOFCs (IT-SOFC), with an operating temperature of 500-700 °C. Among the various available electrolytes, high oxygen diffusivity has been observed for perovskite-based materials. Perovskite structured sodium bismuth titanate ($\text{Na}_{0.5}\text{Bi}_{0.5}\text{TiO}_3$) exhibits high ionic conductivity and transference number. The volatile nature of Bi^{3+} makes NBT a fast ionic conductor. The presence of highly volatile sodium and bismuth makes NBT susceptible to the processing conditions. It exhibits different types of dominant conducting species and nature with slight variation in the concentration and synthesis techniques. Our investigation is focused on the sintering temperature, stoichiometry variation and alteration in the synthesis route of sodium bismuth titanate. Variation from small range hopping to long-range hopping has been suggested with the change in the sintering temperature. Furthermore, a variation from

superlinear behaviour to sublinear behaviour with the change in the Na/Bi ratio has been observed.

Non-stoichiometry in the NBT is considered to be one of the significant issues. To overcome this, we synthesized the sample via liquid phase sintering, i.e. Polyol mediated synthesis. It has been observed that the sample synthesized via Polyol mediated synthesis exhibits better conductivity. Also, the systematic study of Mg substituted $\text{Na}_{0.50}\text{Bi}_{0.49}\text{TiO}_{3-\delta}$ was the focus of the study. The prepared samples were characterized using XRD, SEM, TGA, Raman, and Impedance spectroscopy.

Besides the NBT, Tri-yttrium gallate was also synthesized and systematically investigated for its application as an electrolyte material for IT-SOFC. The structural, morphological, optical and elemental analyses of these systems have been carried out using the XRD, FESEM, UV-Visible and XPS techniques. The impedance analysis technique has been used to investigate the electrical behaviour and conduction mechanism.

In light of the foregoing, we intend to examine a few classes of innovative electrolyte systems that can operate at intermediate temperatures (500-800 °C) while being substantially less expensive. For this purpose, sodium bismuth titanate and triyttrium gallate has been selected as the electrolyte materials. The structural, microstructural, optical, thermodynamical and electrical properties of these materials have been investigated, and the correlation among them is established. This bound volume submitted for the Doctoral degree in IIT BHU comprises seven chapters followed by future work and a list of publications. A brief description is given below:

Chapter 1 deals with the introduction of fuel cells, followed by a brief literature survey. This chapter illustrates the motivation of work, background, and fundamentals of solid oxide fuel cells and the present scenario of electrolyte materials. Moreover, this chapter deals with the various possible conduction mechanism in the investigated systems. The primary goals of the present work are also included in this chapter.

Chapter 2 discusses a detail of the employed experimental instruments and analysis techniques. Solid-state reaction route and polyol mediated synthesis route were adopted to synthesize the samples. This section includes a full description of the instruments used, such as XRD, FESEM, TEM, XPS, DSC, UV-Visible, and Impedance Spectroscopy measurements, as well as significant analysis techniques including Rietveld Refinement and Impedance analysis. The basic physics behind the measurements are also discussed in brief.

Chapter 3 aims to describe the structural properties and ion dynamics of sodium bismuth titanate sample synthesized via solid-state reaction route and sintered at temperature 1000 °C to 1150 °C. Phase formation of NBT was studied by thermal and powder X-ray diffraction techniques. In order to understand the ion dynamics with the sintering temperature, impedance spectra were analyzed. The dc conductivity, hopping frequency and exponent values were extracted from the conductivity spectra analysis. The impedance and modulus spectroscopy along with exponent behaviour suggested short-range hopping for the sample sintered at 1000 °C and followed Ghosh scaling instead of Summerfield scaling. While long-range hopping was observed for the samples sintered at 1150 °C and it followed both the Summerfield scaling and Ghosh scaling. Moreover, the sample is observed to degrade in reducing atmosphere.

Chapter 4 presents the systematic study on the physical properties of substitutional variation in $\text{Na}_{0.5+x}\text{Bi}_{0.5-x}\text{TiO}_{3-\delta}$ ($x = -0.02, -0.01, 0.00, 0.01, 0.02$). It has been observed that Bi

rich compositions exhibit superlinear frequency-dependent behaviour, and Na rich compositions show sub-linear behaviour. To study the degradation mechanism, $\text{Na}_{0.5+x}\text{Bi}_{0.5-x}\text{TiO}_3$ ($x = -0.01, 0.00, 0.01$) samples were kept in reducing environment for 48 h. Further, in order to understand the conduction mechanism and the qualitative/quantitative estimation of charge carriers before and after reducing conditions, various models were used.

In **Chapter 5**, bismuth deficient sodium bismuth titanate, i.e. $\text{Na}_{0.50}\text{Bi}_{0.49}\text{Ti}_1\text{O}_{3-\delta}$, was synthesized using the Polyol mediate synthesis route. This route of preparation helps to produce fine particles, better surface area and good conductivity at relatively lower processing temperatures as compared to the solid-state reaction route. Mg substituted $\text{Na}_{0.5}\text{Bi}_{0.49}\text{Ti}_1\text{O}_{3-\delta}$ samples were found to exhibit higher conductivity as compared to the Bi-deficient samples. A correlation among the phase formation, conduction behaviour and ion diffusion mechanism has also been established for the Mg^{2+} substituted Bi-deficit NBT derived compositions.

Chapter 6 is devoted to the Triyttrium gallate (Y_3GaO_6) based electrolyte systems. Crystal structure, migration path, morphology, thermal properties, conductivity and impedance analysis of all the samples have been discussed employing various characterization techniques. This chapter consists of two sections. In section A, the synthesis of alkaline earth metal substituted Y_3GaO_6 has been studied by the solid-state route and the effect of 2% substitution of Ba, Ca, and Sr on the Y site has been investigated. Section B describes the influence of the higher dopant concentration of Ca on the Y site of Y_3GaO_6 . 2% of calcium substituted Y_3GaO_6 has been found to exhibit the highest conductivity.

Chapter 7 concludes the outcomes of the research works of this thesis and also lists the possibilities of future investigations.